NUMERICAL SIMULATION OF FLOWFIELDS OF THE NAL TWO-DIMENSIONAL TRANSONIC WIND TUNNEL

Kenichi Matsuno*, Nobuyuki Satofuka*
Kyoto Institute of Technology
Norikazu Sudani† and Masahiro Fukuda†
National Aerospace Laboratory

Abstract

Numerical computations of the flowfields of the two-dimensional transonic wind tunnel of the National Aerospace Laboratory, Japan, are presented in this paper. The full Navier-Stokes equations are solved numerically by a cell centered finite-volume method. In the present numerical method the inviscid flux is estimated by the approximate Riemann solver by Roe with MUSCL higher order interpolation, while the viscous flux is approximated by a Galerkin-like discretization formula with the Baldwin-Lomax turbulence model. The present numerical study includes two part: the simulation of the whole flowfield of the wind tunnel and the simulation of the flowfield near the airfoil mounted in the wind tunnel. The computations are compared with the experimental data. The flow mechanism at near-region of an airfoil model mounted in the tunnel is discussed.

Introduction

In two-dimensional transonic airfoil testing, it is important to estimate wall effects on measurement of the flowfields around an airfoil. Experimental studies including flow visualization have been conducted to investigate the flowfields in the NAL(the National Aerospace Laboratory, Japan) two dimensional transonic wind tunnel[1][2]. By these studies, it has become evident that the sidewall boundary layer is large compared with other two dimensional wind tunnel facilities such as the two dimensional wind tunnel of the IAR, Canada. It is found that the presence of the sidewall effects on the flowfield near airfoil surface, especially on the airfoil boundary layer, cannot be ignored. It is important to estimate these effects for airfoil testing. These experimental studies, however, are limited on the flowfield near airfoil. It is difficult to investigate experimentally the whole of the flowfield of the wind tunnel. It is important to know the whole of the flowfield and the characteristics of the wind tunnel well to depict a source of the errors in airfoil testing.

There exist papers presenting numerical simulations on the wind tunnel flowfield[3][4][5]. However, these papers performed the simulations only flowfields of the test section. It, however, is important to investigate the whole of the flowfield in order to understand the top and side wall effects to the measurement.

The purpose of this study is to investigate numerically the whole of the flowfield in the NAL two dimensional transonic wind tunnel of blowdown type. The Navier-Stokes simulation of the flowfield of the NAL two-dimensional wind tunnel is presented in this paper. The computation is performed on whole of the wind tunnel configuration, from a entry of a contraction cone to the exit of the wind tunnel. The detailed computation is also performed for the flowfield near the airfoil model mounted in the tunnel.

The present paper consists of two parts: computation of the flowfield of the whole of the wind tunnel and computation of the flowfield near the airfoil mounted in the wind tunnel. The first part is intended to capture the global flow characteristics of the NAL two dimensional transonic wind tunnel. The next part is the detailed simulation of the near-region of the airfoil model in order to understand the flow mechanism and wall interference.

*Department of Mechanical and System Engineering, Kyoto Institute of Technology, Matsugasaki, Sakyo-ku, Kyoto 606 JAPAN
†National Aerospace Laboratory, Jindaiji-higashi, Chofu, Tokyo 182 JAPAN

Numerical Approach

Governing Equations

The full Navier-Stokes equations governing nonstationary flow are written in the conservation law form as follows:

$$\frac{\partial Q}{\partial t}+\frac{\partial E}{\partial x}+\frac{\partial F}{\partial y}+\frac{\partial G}{\partial z} = \frac{1}{R_e}\left\{\frac{\partial E_v}{\partial x}+\frac{\partial F_v}{\partial y}+\frac{\partial G_v}{\partial z}\right\}, \quad (1)$$

or, in integral form using the Gauss theorem:

$$\frac{\partial}{\partial t}\int_\Omega Q dV+\int_{\partial\Omega}(H-H_v)dS=0. \quad (2)$$

where,

$$H = En_x+Fn_y+Gn_z,$$

$$H_v = \frac{1}{R_e}(E_v n_x+F_v n_y+G_v n_z).$$

Here, Ω is a control volume or a cell, $\partial\Omega$ is a cell surface, and (n_x, n_y, n_z) is unit vector normal to the cell surface. The dependent variables $Q=(\rho,\rho u,\rho v,\rho w,e)^T$ is the vector of the conservative variables. H and H_v are the inviscid and viscous fluxes, respectively.

Cell-centered Finite-Volume Method

We use the structured mesh system: (ξ,η,ζ). The cell-centered finite volume formulation is applied to Eq.(2), where the integral is estimated about the cell (i,j,k).

Now the Eq.(2) is discretized at the time level $n+1$, assuming that the states at the time-level up to n are completely known. Then we get the following discretized equation:

$$\left[\frac{\Delta QV}{\Delta t}\right]_{i,j,k}+\sum_{l=i,j,k}\delta_l(H-H_v)_l^{n+1}\Delta s_l=0, \quad (3)$$

where,

$$\delta_l H_l\Delta s_l = H_{l+1/2}\Delta s_{l+1/2}-H_{l-1/2}\Delta s_{l-1/2}$$

$$\Delta Q = Q^{n+1}-Q^n, \qquad (l=i,j,k).$$

Here, the time-step is represented by Δt and $V_{i,j,k}$ is the volume of the cell (i,j,k). $\Delta s_{l+1/2}$ is the area of the cell interface in the l-direction, $l=i,j,\mathrm{or}k$.

The inviscid flux at the cell interface $H_{l+1/2}$ is evaluated by the Roe's flux difference splitting[6] as

$$H_{l+1/2}=\frac{1}{2}\left[H(Q^R)+H(Q^L) -|\bar{P}^{Roe}_{l+1/2}|(Q^R-Q^L)\right]. \quad (4)$$

The variables at cell interface Q^L and Q^R are evaluated by the high-order MUSCL interpolation[7] with the *minmod* limiter using the primitive variables (ρ,u,v,w,p). The third-order accurate MUSCL interpolation is used throughout the paper. The matrix $\bar{P}^{Roe}_{l+1/2}$ is evaluated with the Roe averaged-state variables, which are denoted by $\overline{()}$, such that

$$H(Q^R)-H(Q^L)=\bar{P}^{Roe}(Q^R-Q^L),$$

and $|\bar{P}^{Roe}|$ is defined as

$$|\bar{P}^{Roe}|=\bar{R}|\bar{\Lambda}|\bar{R}^{-1}.$$

Here, $\bar{\Lambda}$ is the diagonal matrix whose elements are the eigenvalues of the matrix P^{Roe} and R is the matrix whose columns are the right eigen vectors of these eigenvalues.

The viscous flux term at the cell interface is evaluated by Galerkin-like discretization which results the formula of central-difference method.

The implicit flux vecters of the Eq.(3) are now linearized by

$$\begin{aligned} H^{n+1} &= H^n+\left(\frac{\partial H}{\partial Q}\right)^n\left(Q^{n+1}-Q^n\right) \\ &= H^n+P^n\Delta Q. \end{aligned} \quad (5)$$

Introducing these linearized flux terms into Eq.(3), we get

$$\left[I+\frac{\Delta t}{V_{i,j,k}}\sum_{l=i,j,k}\delta_l(P^n-P_v^n)_l\Delta s_l\right]\Delta Q_{i,j,k} = -\frac{\Delta t}{V_{i,j,k}}[RHS]_{i,j,k} \quad (6)$$

$$[RHS]_{i,j,k}=\sum_{l=i,j,k}\delta_l(H-H_v)_l^n\Delta s_l.$$

In this paper, the steady flow solutions are sought for and the expensive penta-diagonal

solver should be avoided from the efficiency considerations. Thus, the Jacobian matrices appearing in the left-hand side of the above equation may be approximated. The first order upwind formulas are used for the flux terms in the implicit side of Eq.(6) in order to make the system tridiagonal. Thus, in the left-hand side of the Eq.(6), $\Delta Q^L_{l+1/2}$ and $\Delta Q^R_{l+1/2}$ are estimated by ΔQ_l and ΔQ_{l+1}, respectively. The viscous-flux Jacobian P_v appearing left-hand side of Eq.(6) is omitted for simplicity. Furthermore both the approximate-factorization and diagonalization techniques proposed by Pullium and Chausee[8] are introduced for efficiency. Thus final formula of the present finite volume method becomes:

$$
\begin{aligned}
R_i \left[I + \frac{\Delta t}{V_{i,j,k}} \delta_i \left(\Delta s_i \Lambda_i \right) \right] R_i^{-1} \\
\times R_j \left[I + \frac{\Delta t}{V_{i,j,k}} \delta_j \left(\Delta s_j \Lambda_j \right) \right] R_j^{-1} \\
\times R_k \left[I + \frac{\Delta t}{V_{i,j,k}} \delta_k \left(\Delta s_k \Lambda_k \right) \right] R_k^{-1} \\
\times \Delta Q_{i,j,k} \\
= - \frac{\Delta t}{V_{i,j,k}} \left[RHS \right]_{i,j,k} . \qquad (7)
\end{aligned}
$$

The computation is started with proper initial condition and the steady state solution is obtained in a time-dependent manner.

Numerical Boundary Conditions

The boundary conditions needed for the present cell-centered finite volume method (7) are set by use of fictitious cells placed outside of the boundary or inside of the body-wall. Individual boundary condition of the problems will be given at the corresponding sections.

Code Verification

At first, the accuracy and verification of the code are checked by comparison with experimental data and the other computation. Two dimensional flow around NACA0012 airfoil is adopted in the comparison, though the present computer code is written for three dimensional flows. Therefore we put four grid points in the span direction with periodic boundary treatment, while a C-type grid of 249 (181 on airfoil surface) grid points in ξ-direction and 60 grid points with minimum spacing of 3.3×10^{-6} is used. The transition point from laminar to turbulent is fixed at 5 % chord point. The Baldwin-Lomax turbulence model is used for estimation of eddy viscosity. The purpose of this computation is to check the reliability of the code and accuracy of the computed results. Computation was carried out at a Mach number of uniform flow $M_\infty = 0.7$, Reynolds number based on the airfoil chord length $Re_\infty = 9.0 \times 10^6$, angle of attack $\alpha = 1.49°$. Figure 1 shows comparison of the present result with the experiment by Harris[9]. Table 1 shows the comparison of the computed lift coefficient C_L and drag coefficient C_D with experiment[9] and computation by Coakley[10].

Table 1. Comparison of C_L and C_D.

	C_L	C_D
Present	0.246	0.0084
Experiment(Harris)	0.241	0.0079
Computation(Coakley)	0.255	0.0083

From these comparison, the present result agrees well with the other computation and experiment, which shows partly the verification of the present code and the accuracy of the method.

Wind-Tunnel Simulation, Results and Discussion

All the calculation in this paper were carried out with third-order accurate MUSCL interpolation. Convergency was checked by monitoring the residual of right-hand side of the method.

Two-Dimensional Transonic Wind Tunnel

The NAL two-dimensional wind tunnel[11] was built to meet the requirements of high Reynolds number testing of wing section at transonic regime. It is a blowdown tunnel with a test section of 0.3 m × 1.0 m. The capability of the tunnel is for Mach numbers from 0.2 to 1.2 and for a Reynolds number up to 40 million at Mach number 0.8. Figure 2 shows the tunnel. The air from 20.5 kg/cm^2 high pressure air tank flows through pressure regulating valve and settling chamber, where the flow disturbances are removed, and reaches to contraction cone. At this contraction cone of length $3m$, the cross section of the flow path is changed from a circular of diameter $2.5m$ to a rectangular of $1.0m \times 0.3m$. Overall contraction ratio is 16.35:1. The test section follows the contraction cone. The test section is $0.3m$ wide, $1.0m$ high and $3.0m$ long. It is enclosed in the

plenum chamber of a $2.8m$ diameter. Top and bottom walls are slotted walls with variable open-area ratio of zero to ten percent. The side walls are solid. The air through test section flows into second throat, locating at the $3.6m$ downstream of the test section and exits to outside of the facility through a silencer.

The present numerical simulation covers the region from contraction cone to downstream of the test section, where the tunnel flow characteristics is considered to be determined directly. The test section with an airfoil model is also focused and detailed simulation is performed.

Overall Flowfield Solution

The first simulation was performed for understanding the flow characteristics of the whole of wind tunnel which were considered to be determined by the tunnel configuration. The simulation in this section covers the region from the entry of the contraction cone to the downstream of the test section. In the present simulation, it is assumed that a NACA0012 airfoil model is mounted at the test section with zero angle of attack.

Computational Grid

The computation region includes some special feature in the geometry. The cross section is circular at the upstream of the contraction cone and rectangular at the test section of the tunnel. The cross section geometry of the contraction cone changes its shape gradually from the circle at the entry to the rectangle at the exit of the contraction cone. The airfoil model is also mounted in the test section whose cross section is rectangular. It is important to consider these geometric condition for generating the computational grid. The most important issue in the grid system, the regions at the boundary-layers at the four walls should not include the irregular point of the grid system from the solution-accuracy and stability considerations. The grid system of simple topology shown in Figs.3(a), (b) and (c) is used in this computation. In the figures, the shape of the tunnel duct and plenum chamber are illustrated using solid lines. The NACA0012 airfoil model is assumed to be mounted at zero angle of attack in the test section. The symmetry assumption as to the horizontal plane is forced in order to save the grid points in the computation. The number of the grid points is 105 in the flow ($i-$) direction, 18 in the radial/wing-span ($j-$) direction, and 54 along the wall ($k-$direction) (total 102,060 grid points).

Numerical Computation

The initial condition for impulsive start of the computation is as follows; The Mach number at the test section of the tunnel is given. The one-dimensional isotropic flow according to the variation of the cross-sectional area is calculated and given as the initial flow condition. The total temperature T_0 and entropy s_0 at the entry of the contraction cone estimated above are also used as the boundary condition. The boundary conditions of the computation are as follows. At the entry of the contraction cone, the inflow boundary conditions are specified. In the present computation, the total temperature T_0 and entropy s_0 are specified and other quantities are derived using the one-dimensional Riemann invariants and first-order extrapolation. At the exit of the test section, the out-flow boundary conditions are given. The pressure p_{ex} at the exit is specified explicitly and other quantities are derived from the Riemann invariant and first-order extrapolation. At the surfaces of the wind-tunnel walls and airfoil model, no slip boundary condition is used, and the non-heat transfer ($\partial T/\partial n = 0$) is assumed.

Due to the insufficiency of the grid points especially toward the $j-$direction, it is assumed in this computation that the flow is laminar. Thus the Reynolds number based on the airfoil-chord length is assumed 10^5 and the Mach number at the test section of the tunnel is 0.8. The effect of the existence of the plenum chamber is not included and the upper and lower slotted walls of the test section are assumed to be closed.

Figure 4 shows the surface grid as well as the surface-pressure contours on the contraction cone. Figure 5 shows the pressure contours on the (a) vertical and (b) horizental symmetry planes. Figures 6(a) and (b) show the contours of the density and Mach number on the horizontal plane, respectively. From these figures, the typical pressure distribution near the airfoil model is attained. The two-dimensionality is attained at the center of the airfoil model. No flow-separation at the entry or the exit of the contraction cone appears. As for the contraction cone of the wind tunnel, the pres-

sure distribution, density distribution, and Mach number distribution show the favorable flow characteristics. The two-dimensionalty is predicted near the vertical symmetry region or center region of the test section, though only 18 cell grids are put in the airfoil-model-span direction. There exists no special problem in the calculated flow properties in the present computational conditions. However, the separation at the junction region between airfoil model and side wall of the tunnel does not appear in the present computation, because the very coarse grid points are put in the airfoil-model-span direction. It is evident too coarse to catch such the separation.

It is very important to get the information on that region in order to discuss the two-dimensionality and the flow characteristics. Thus to capture the details of the flow mechanism near the airfoil model region, the computation on that region was performed and the results is given at the following section.

Test-Section Flowfield Solution

The computation in this section was performed for the purpose of capturing flow details at the airfoil model region. In order to put adequate grid cells at the region, the computation was performed with another situation, independently of the previous section. We have enough data of experiment of a BGK No.1 airfoil conducted at the NAL[1][2][12]. Thus, the BGK No.1 airfoil model is assumed to be mounted in the tunnel. Two-dimensionalty of the computed flowfield is compared with experiment.

Computational Grid

Vertical symmetry is assumed in the computation to save the grid points. Therefore the half of the test section is considered for computation. Figure 7 shows the computational grid of this computation. The C-type of $109 \times 34 \times 40$ grid cells are used. Minimum spacing of the grid is 1.0×10^{-6} at the adjacent grid of the side wall and airfoil.

Numerical Computation

Computation is performed under the conditions that the free-stream Mach number is $M_\infty = 0.75$, the Reynolds number based on the airfoil chord length $Re_\infty = 21.0 \times 10^6$, the angle of attack $\alpha = 2.0°$, the airfoil-model aspect ratio (span length/chard length) is 1.2. The slotted walls of the ceiling and floor are assumed 3 % of the open-area ratio in the simulation.

The turbulent eddy viscosity is estimated by the Baldwin-Lomax turbulent model. The extension of the turbulence model to the three dimensional space follows Vatsa and Weden[5].

From the detailed measurement of the boundary layer on the tunnel side-wall, the NAL two-dimensional transonic wind tunnel has relatively thick side-wall boundary layer compared with other wind tunnel. The displacement thickness δ^* of the side-wall boundary layer is $4.7mm$ at the test section. In the present computation, two dimensional computation about the flow past flat plate were performed in advance and the calculated boundary layer properties which are according to the measured displacement thickness ($\delta^* = 4.7mm$) are used as the boundary condition of the side-wall boundary-layer at the inflow position. The other treatment of the inflow and outflow boundary conditions are the same as the previous tunnel-flow simulation. The upper(ceiling) and lower (floor) walls have 3 % opening of the slotted wall. Thus the present computation allows the through passage of the rate of 3 % of the momentum in the vertical direction. The other component of the flow properties are put as like as slip-wall condition.

Figure 8 shows the isobars on the airfoil surface and side wall. The figure shows good two-dimensionality near and at the center of the airfoil model. Figure 9 shows the chordwise distribution of the airfoil-surface pressure at various span position ($y/(b/2) = 0,\quad 0.5,\quad 1.0, b = 30cm$:full span length). Here, $y = 0$ is the position of the vertical symmetry plane or the center of the airfoil model. The pressure distribution on $y = 0$ line is also compared with the experiment in Fig.9. Comparison of the computed pressure distribution in the airfoil-span direction with experiment is shown in Fig.10. The agreement is good. Both the experimental data and computed result show good two-dimensionalty.

Summary and Conclusion

The Navier-Stokes simulations of the flowfields

of the NAL two-dimensional transonic wind tunnel were presented in this paper. The flowfield of the wide range of the wind tunnel facility, from the contraction cone to the downstream of the test section, was treated and simulated. The detailed simulation of the flowfield near the airfoil model mounted in the tunnel was also performed. The comparisons of the numerical results with the experiment shows very good agreement.

The combination of the two computation using overset grid methodology is now under development and will be appear in near future.

References

(1) N.Sudani, M.Sato, H.Kanda and K.Matsuno, Flow Visualization Studies on Sidewall Effects in Two-Dimensional Transonic Airfoil Testing, J. of Aircraft, Vol.31, (1994), 1233-1239.

(2) M.Sato, H.Kanda, N.Sudani, and K.Matsuno, Oil Flow Visualization Studies of Sidewall Effects in Transonic Airfoil Testing, NAL TR-1196, (1993) (in Japanese).

(3) S. Obayashi and K. Kuwahara, Navier-Stokes Simulation of Side Wall Effect of Two-Dimensional Transonic Wind Tunnel, AIAA Paper 87-0037, (1987).

(4) J.E.Deese, J.G. Jhonson, R.K. Agarwal, B.K. Soni, and R.C. Crites, Simulation of Wind Tunnel Flowfields, AIAA Paper 92-0034, (1992).

(5) V.N. Vatsa and B.W. Bedan, Navier-Stokes Solutions for Transonic Flow Over a Wing Mounted in a Tunnel, AIAA Paper 88-0102, (1988).

(6) P.L.Roe, Approximate Riemann Solvers, Parameter Vectors, and Difference Schemes, J. Comp. Phys., Vol.43, (1981), pp.357-372.

(7) B.van Leer, Towards the Ultimate Conservative Difference Scheme. V. A Second Order Sequel to Godunov's Method J. Comp. Phys., Vol.32 (1979), pp.101-136.

(8) Pulliam, T. H. and Chaussee, D. S., A Diagonal Form of an Implicit Approximate-Factorization Algorithm, J. Comp. Phys., Vol.39, No.2, (1981), pp.347-363.

(9) C.D. Harris, Two-Dimensional Aerodynamics Characteristics of The NACA0012 Airfoil in the Langlay 8-Foot Transonic Pressure Tunnel, NASA TM-81927. (1981).

(10) T.J. Coakley, Numerical Simulation of Viscous Transonic Airfoils, AIAA paper 87-416, (1987).

(11) Staff of 2nd Aerodynamics Division, Construction and Performance of NAL Two-Dimensional Transonic Wind Tunnel, NAL TR-647T, (1982).

(12) N. Sudani, K. Matsuno, H. Kanda, M. Sato, H. Miwa, and I. Kawamoto, A Comparative Study of BGK No.1 Airfoil Sata in High Reynolds Number Transonic Wind Tunnels, NAL TR-1191T, (1993).

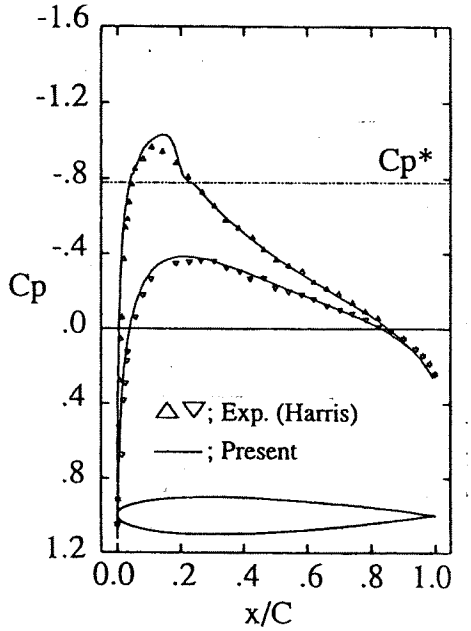

Figure 1 Comparison of the pressure coefficient with experiment.

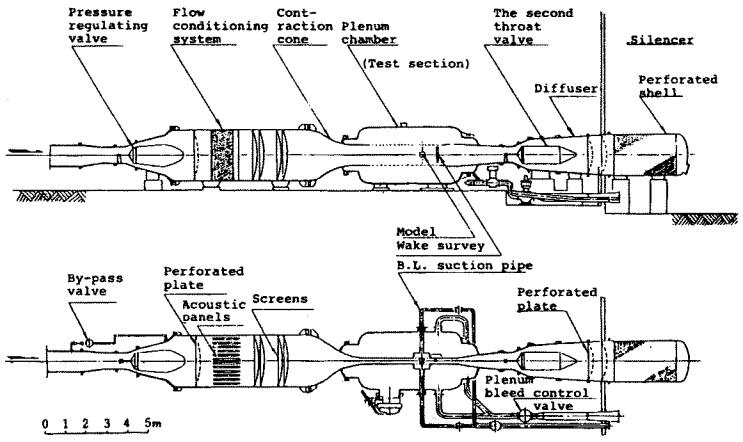

Figure 2 Schematic diagram of the NAL2-D transonic wind tunnel. The side view(upper) and top view(lower).

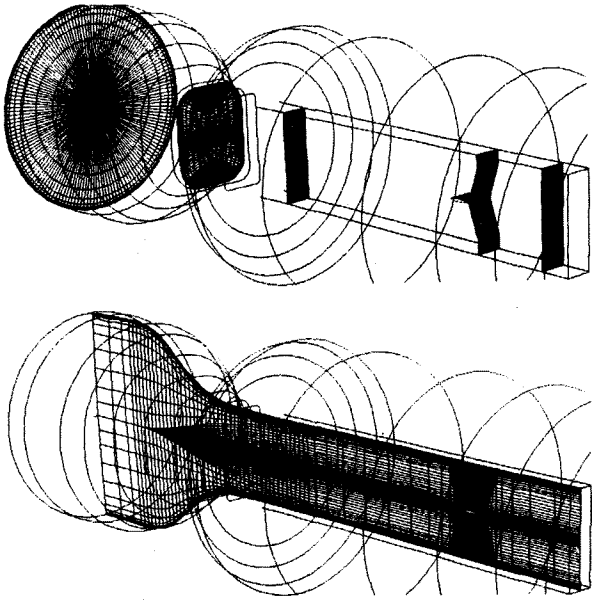

Figure 3 (a)-*upper* : Grid at various cross sections.(Airfoil-surface grid is also shown).
(b)-*lower* : Grid on vertical symmetry plane

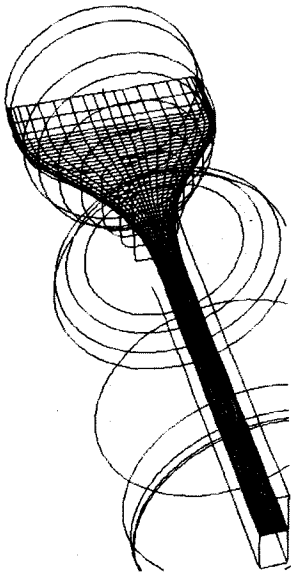

Figure 3(c) Computational grid at horizontal symmetry plane, view from upper side.

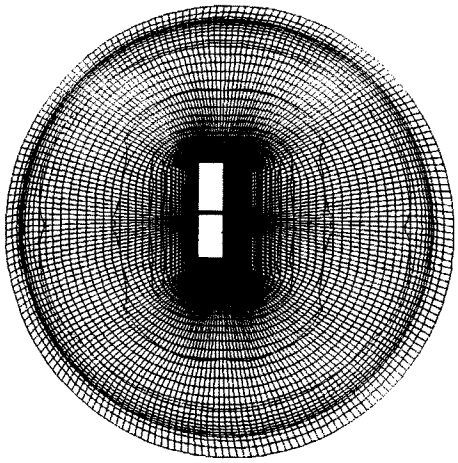

Figure 4 Surface grid and pressure contours on the contraction cone, view from upstream of the entry of the contraction cone.

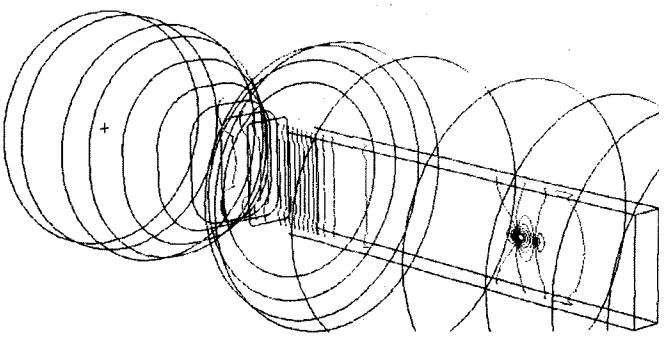

Figure 5 (a) Pressure contours on the vertical symmetry plane of the tunnel.

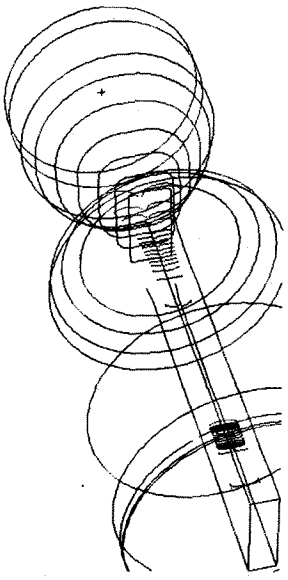

Figure 5 (b) Pressure contours on the horizental symmetry plane of the tunnel.

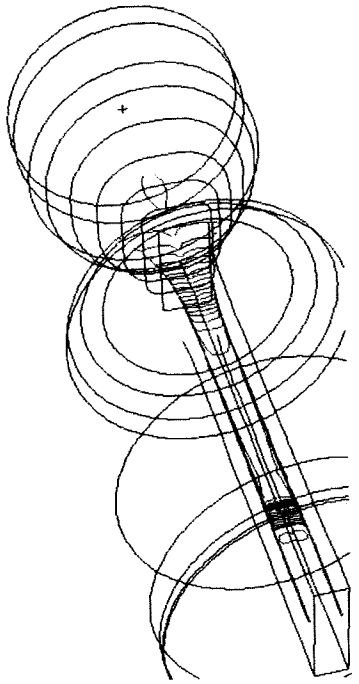

Figure 6(a) Density contours on the horizontal symmetry plane of the tunnel.

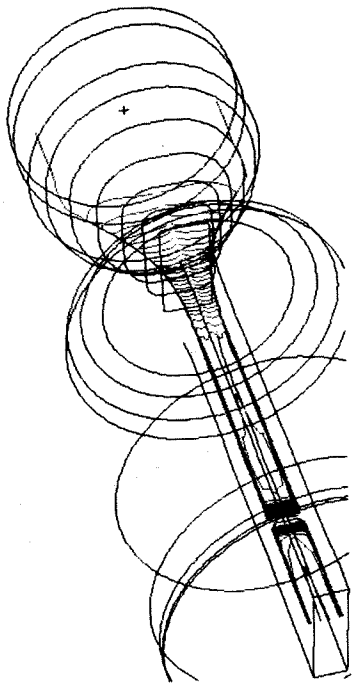

Figure 6(b) Mach number contours on the horizontal symmetry plane of the tunnel.

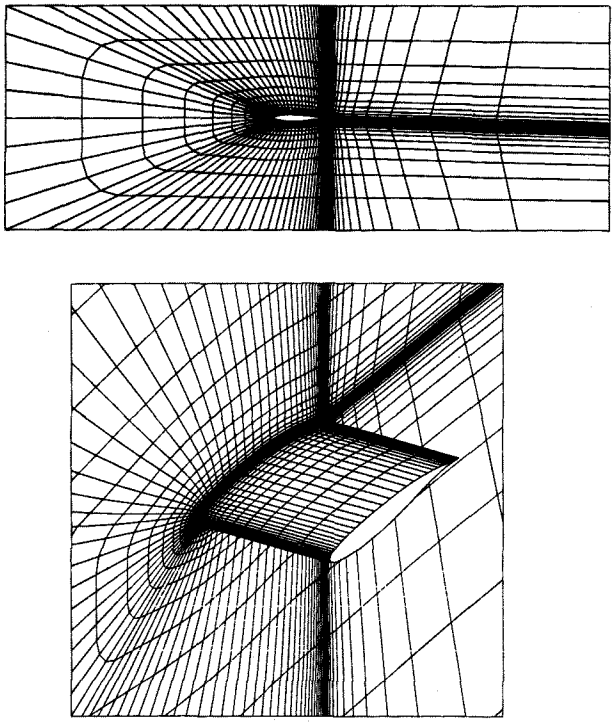

Figure 7 Computational grid. (a)-*upper* : Over all, side view, (b)-*lower* : Close up at the airfoil-wall junction region

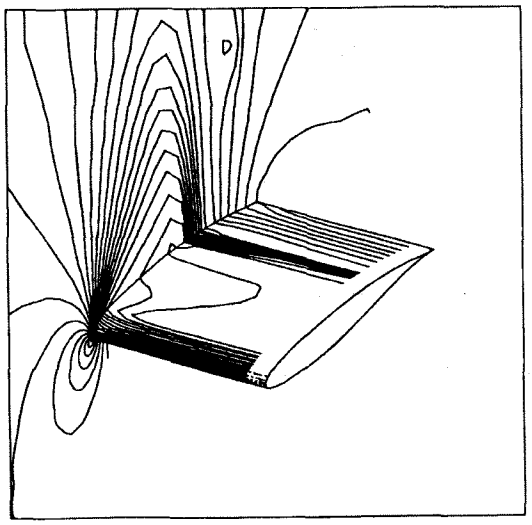

Figure 8 Isobars on the airfoil surface and side wall, shown half of the model.

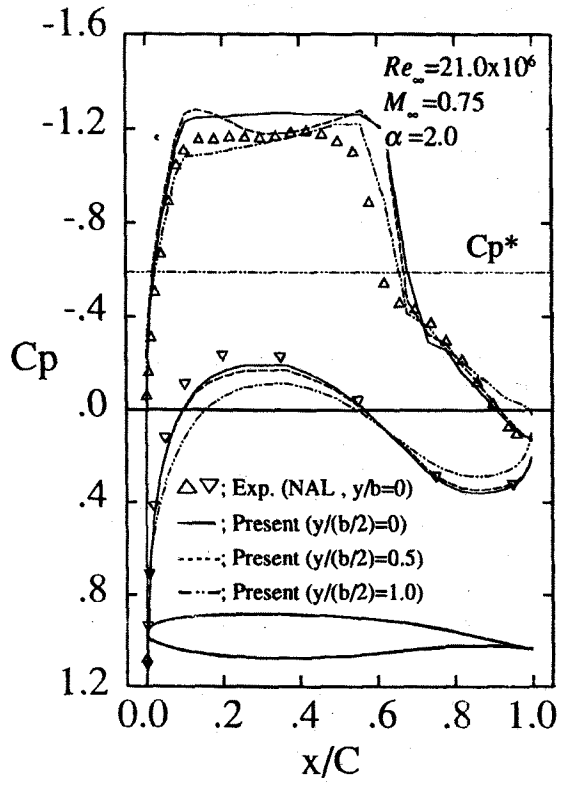

Figure 9 Chordwise airfoil-surface pressure distribution at various span positions.

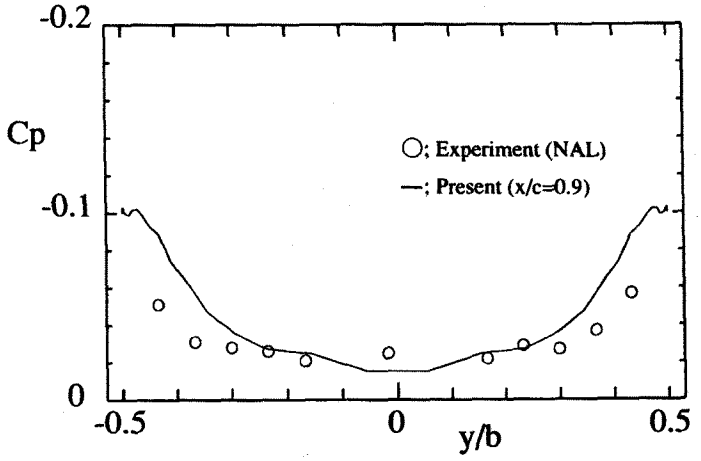

Figure 10 Spanwise airfoil-surface pressure distribution at the 90 % chord position.